Computers & Geosciences 103 (2017) 12–20

Contents lists available at ScienceDirect

Computers & Geosciences

journal homepage: www.elsevier.com/locate/cageo

Research paper

Mechanical properties and energy conversion of 3D close-packed lattice model for brittle rocks

Chun Liu[a,b,c,*], Qiang Xu[b], Bin Shi[a], Shang Deng[c], Honghu Zhu[a,d]

[a] School of Earth Sciences and Engineering, Nanjing University, Nanjing 210023, China
[b] State Key Laboratory of Geohazards Prevention and Environment Protection, Chengdu University of Technology, Chengdu 610059, China
[c] Department of Geological and Environmental Sciences, Stanford University, Stanford, CA 94305, USA
[d] Nanjing University (Suzhou) High-Tech Institute, Suzhou 215123, China

ARTICLE INFO

Keywords:
Discrete element model
Mechanical property
Energy
Heat
MatDEM

ABSTRACT

Numerical simulations using the 3D discrete element method can yield mechanical and dynamic behaviors similar to rocks and grains. In the model, rock is represented by bonded elements, which are arranged on a tetrahedral lattice. The conversion formulas between inter-element parameters and rock mechanical properties were derived. By using the formulas, inter-element parameters can be determined according to mechanical properties of model, including Young's modulus, Poisson's ratio, tensile strength (T_u), compressive strength (C_u) and coefficient of internal friction. The energy conversion rules of the model are proposed. Based on the methods, a Matlab code "MatDEM" was developed. Numerical models of quartzite were used to validate the formulas. The tested mechanical properties of a single unit correspond reasonably well with the values of quartzite. Tested T_u and C_u with multiple elements are lower than the values predicted by the formulas. In the simulation of rock failure processes, mechanical energy conversed between different forms and heat is generated, but the mechanical energy plus heat always remains constant. Variations of breaking heat and frictional heat provide clues of the fracturing and slipping behaviors of the T_u and C_u tests. The model may be applied to a wide range of geological structures that involve breakage at multiple scales, heat generation and dynamic processes.

1. Introduction

The discrete element method (DEM) was first introduced by Cundall and Strack (1979) to study the behavior of granular assemblies. The method was improved to a close-packed lattice solid model that has been used in the numerical simulation of the dynamical processes associated with earthquakes (Mora and Place, 1993, 1994). And a bonded discrete element model was proposed to simulate the behaviors of cohesive material (Mora and Place, 1998; Potyondy et al., 1996). The method permits large relative motion inside the model, non-linear behaviors and dynamic evolution (Hazzard et al., 2000). Therefore, it has been widely used in the simulation and interpretation of various geological phenomenon that involve breakage and discontinuities, such as earthquake faults with gouge (Guo and Morgan, 2007, 2008; Mora and Place, 1998), fault-propagation folding (Hardy and Finch, 2006), structural evolution of calderas (Hardy, 2008), faulting over active salt diapir (Yin et al., 2009), compaction bands (Dattola et al., 2014), growth fault (Chu et al., 2015), and extension fracture propagation in rocks with veins (Virgo et al., 2013).

In the DEM, rock is represented by an assemblage of a series of bonded discrete elements. Generally, the modeling method relies on troublesome calibration processes to determine the correct inter-element parameters (Boutt and McPherson, 2002; Cho et al., 2007; Kazerani and Zhao, 2010; Potyondy and Cundall, 2004; Schopfer et al., 2009). Tavarez and Plesha (2007) investigate the Young's modulus and Poisson's ratio of the 2D close-packed model. And Asahina et al. (2015) simulate the deformation of lattice model with arbitrary Poisson's ratio. The model has analytical elastic solutions (Griffiths and Mustoe, 2001; Hoover et al., 1974; Liu et al., 2013; Wang et al., 2000), which may provide a theoretical basis for calibration of inter-element parameters. The elastic properties of close-packed 3D lattice model have been investigated by Wang and Mora (2008). However, relations that specify bond strengths in terms of macroscopic strengths have not been reported (Ergenzinger et al., 2011). The relationship between micro inter-element properties and macro mechanical properties of 3D lattice model is not necessarily clear.

Failure processes of rock, such as faulting and earthquake dynamics, involve complicated friction, fracture, granular flow, wave

* Corresponding author at: School of Earth Sciences and Engineering, Nanjing University, Nanjing 210023, China.
E-mail address: chunliu@nju.edu.cn (C. Liu).

http://dx.doi.org/10.1016/j.cageo.2017.03.003
Received 4 August 2015; Received in revised form 26 February 2017; Accepted 1 March 2017
Available online 03 March 2017
0098-3004/

propagation and energy conversion. Discrete element models have been applied to simulate faulting and earthquake phenomena (Abe and Mair, 2009; Fournier and Morgan, 2012; Latham et al., 2006; Mora and Place, 1993, 1994). Elastic potential energy is stored as tectonics stress when Earth's crust deforms. When a fault slips, the stored energy is suddenly released as seismic waves and heat (Mora and Place, 1993). The energy released may trigger other events and therefore have an effect on the damage incurred by the rock (Hazzard and Young, 2004; Hazzard et al., 2000; Michlmayr et al., 2013). The calculation of energy of the model provides an alternative way to study the causes of seismic wave attenuation, frictional heat generation, and failure zone evolution (Mora and Place, 1998; Place et al., 2002). Kinetic energy and elastic potential energy have been used to realize the process of faulting and induced seismicity (Latham et al., 2006), such as the stick-slip frictional behavior (Mora and Place, 1993). Place and Mora (1999) model the generation of frictional heat during faulting. However, the accuracy of the heat calculation is influenced by internal friction, and the calculated heat may be up to 10 times less than the theoretical value (Mora and Place, 1998; Place and Mora, 1999).

In this 3D discrete element model, rock is represented by bonded elements, which are arranged on a tetrahedral lattice packing. A tetrahedral unit with four elements was used to derive the conversion formulas between inter-element parameters and mechanical properties of the model. The energy conversion rules of the model are proposed, in order to simulate the energy conversion and heat generation during failure and dynamic processes of rocks. A Matlab code "MatDEM^{3D}" has been developed and numerical models of quartzite were used to validate the formulas and the model. The energy conversion and heat generation were simulated during the failure of the model. Note that, we do not stipulate a discrete element to represent a single rock grain in this paper, but rather, the assemblage of discrete elements represents a collection of spatially averaged grains (Boutt and McPherson, 2002).

2. The 3D close-packed model

The 3D discrete element model used in this study is based on the lattice solid model (Mora and Place, 1993, 1994). As shown in Fig. 1a, the elements used in the model are identical, which are hexagonal close packing (HCP). The elements interact through a spring force (Fig. 1b), in which the normal force (F_n) between two elements is defined as the product of normal stiffness (K_n) and normal relative displacement (X_n) (Hardy and Finch, 2006; Yin et al., 2009). The spring bond between two elements is originally intact, until X_n between the element pair exceeds the breaking displacement (X_b), whereupon the bond breaks, and the tensile force ceases to exist between them. However, the repulsive force still acts between the two elements when they return to a compressive contact.

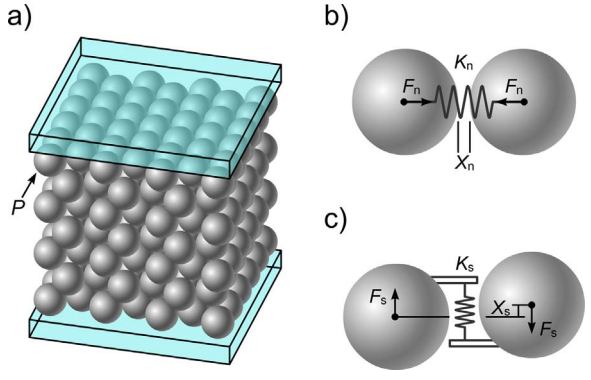

Fig. 1. (a) A 3D close-packed lattice model (hexagonal close packing). (b) Two elements are bonded by a breakable elastic spring and interact through a spring force. (c) Two elements also are bonded by a spring along the tangential direction to simulate the shear deformation and shear force.

As shown in Fig. 1c, two elements are assumed to be bonded by breakable elastic springs along the tangential direction, to simulate shear deformation and shear force. The shear relative displacement is the relative displacement of two elements along the plane perpendicular to the connection line of their centers. Similarly, the inter-element shear force (F_S) is defined as the product of shear stiffness (K_s) and shear relative displacement (X_s) (Cundall and Strack, 1979; Hardy et al., 2009). For cohesive materials, such as soil and rock, there is a cohesion between units, which is independent of the normal effective stress. Therefore, the maximum shear force (F_{Smax}) of an intact bond allowed by Coulomb friction is:

$$F_{S\,\max} = Fs_0 - \mu_p \cdot F_n \tag{1}$$

where Fs_0 is the inter-element initial shear resistance; μ_p is the inter-element coefficient of friction; F_n is the normal force (compressive force is negative). The Fs_0 is the maximum shear force, when the normal force (F_n) is zero. The shear relative displacement and shear force increase with increasing external shear force. The intact bond between two elements will break when the external force exceeds the F_{Smax} of Eq. (1). Then, the magnitude of the shear force (F_S) is limited to be less than or equal to the maximum shear force (F_{Smax}') of the broken bond, $-\mu_p \cdot F_n$. When the bond is broken and the magnitude of external shear force exceeds the limit F_{Smax}', two elements begin slipping, and the slipping friction between the element pair is F_{Smax}'.

3. Mechanical properties of the 3D model

3.1. Deformation of basic tetrahedral unit

The basic tetrahedral unit shown in Fig. 2a is used to investigate the mechanical properties of the model. In the unit, four identical elements are bonded to each other. The centers of the elements 1–4 are originally located at points A~D, respectively. In Fig. 2b, the z-coordinate of elements 2, 3 and 4 is fixed to simulate rigid smooth boundary. An external force, Fz acts on the element 1, which moves upward by a very small displacement dz to point A'. In response to the tensile force, the centers of the elements 2, 3 and 4 move toward the center point (O) of the equilateral triangle BCD to points B', C' and D', respectively. When the displacements are very small, the deformation of the tetrahedral unit has analytical solutions, and dz, X_{n1}, X_{s1} and X_{n2} can be expressed as (details in Appendix A):

$$dz = \frac{5K_n + K_s}{9K_n(K_n + K_s)} \cdot Fz \tag{2a}$$

$$X_{n1} = \frac{\sqrt{6}(3K_n + K_s)}{18K_n(K_n + K_s)} \cdot Fz \tag{2b}$$

$$X_{s1} = \frac{2\sqrt{3}K_n}{9K_n(K_n + K_s)} \cdot Fz \tag{2c}$$

$$X_{n2} = -\frac{\sqrt{6}(K_n - K_s)}{18K_n(K_n + K_s)} \cdot Fz \tag{2d}$$

3.2. Young's modulus and Poisson's ratio

By using Eqs. (2d) and (2a), the normal strains of the unit along the x-direction (ε_{xx}) and z-direction (ε_{zz}) are defined by:

$$\varepsilon_{xx} = \frac{X_{BO}}{l_{BO}} = \frac{X_{n2}}{l_{BC}} = -\frac{\sqrt{6}(K_n - K_s)}{18K_n(K_n + K_s)} \cdot \frac{Fz}{d} \tag{3a}$$

$$\varepsilon_{zz} = \frac{dz}{l_{AO}} = \frac{\sqrt{6}(5K_n + K_s)}{18K_n(K_n + K_s)} \cdot \frac{Fz}{d} \tag{3b}$$

where d is the edge length for the tetrahedral lattice unit, i.e. the diameter of element; X_{BO} is the displacement of element 2 along line

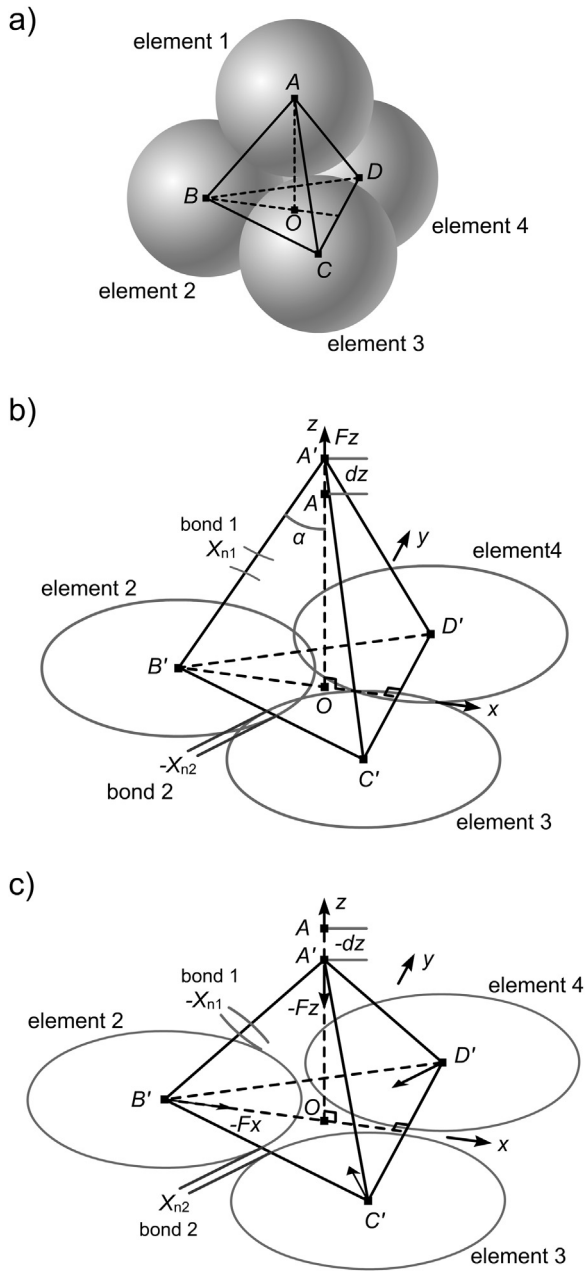

Fig. 2. (a) In a tetrahedral unit, four elements are bonded to each other. (b) A vertical force *Fz* acts on the unit, which is stretched in the vertical direction and shrinks laterally. (c) Horizontal bonds (e.g. bond 2), break when the relative displacement (X_{n2}) between bottom elements exceeds the breaking displacement. A vertical compressive force *Fz* and horizontal compressive forces (e.g. *Fx*) act on the unit.

BO; l_{BO}, l_{BC} and l_{AO} are the lengths of segments *BO*, *BC* and *AO*, respectively. Therefore, the vertical Poisson's ratio (υ) can be calculated by:

$$\upsilon = -\frac{\varepsilon_{xx}}{\varepsilon_{zz}} = \frac{K_n - K_s}{5K_n + K_s} = \frac{1-\gamma}{5+\gamma} \tag{4}$$

where γ is the ratio of shear stiffness to normal stiffness. The equation indicates that υ decreases with increasing γ. Since the stiffness is always positive, the maximum υ of the 3D model is 0.2 when γ is 0. When γ=1, it corresponds to a material with zero Poisson's ratio.

Let S_{BCD} represents the area of the triangle BCD. In the *xy* plane, each unit occupies an area of $2{\cdot}S_{BCD}$, and the vertical stress (σ_{zz}) is defined by:

$$\sigma_{zz} = Fz/(2{\cdot}S_{BCD}) = 2\sqrt{3}\,Fz/(3d^2) \tag{5}$$

With Eqs. (3b) and (5), the vertical Young's modulus (E) can be expressed as:

$$E = \sigma_{zz}/\varepsilon_{zz} = \frac{6\sqrt{2}\,K_n(K_n + K_s)}{d(5K_n + K_s)} \tag{6}$$

Eqs. (4) and (6) are consistent with the simulated results of previous works (Boutt and McPherson, 2002; Hazzard et al., 2000; Neveu et al., 2016), that Young's modulus increases with increasing normal stiffness and the ratio of the shear to normal stiffness (γ) influences Poisson's ratio (Potyondy and Cundall, 2004). The two equations also were obtained by Wang and Mora (2008) using a different approach based on strain energy density. However, the new method based on the small deformation assumption has inherent advantages in the investigation of the failure modes of the close-packed model, which is more important in applications.

3.3. Tensile strength

In the basic unit of Fig. 2b, with increasing tensile force *Fz*, the normal relative displacements of inclined bonds (e.g. X_{n1}) increase, until the bonds break in opening mode (when $X_{n1} > X_b$). Substituting Eq. (2b) into Eq. (5), and let X_{n1}=X_b, the tensile strength (T_u) of the unit can be expressed as:

$$T_u = \frac{6\sqrt{2}\,K_n(K_n + K_s)}{3K_n + K_s} \cdot \frac{X_b}{d^2} \tag{7}$$

3.4. Compressive strength

Microscopic observation of laboratory rock and crystal samples has shown that most cracks that form during uniaxial compressive tests are tensile and sub-parallel to the maximum compressive stress (Hallbaue et al., 1973). The eventual failure of the sample must occur by linking up of the tensile cracks to form a macroscopic shear facture (Horii and Nematnasser, 1985). In the model, the appearance of tensile cracks corresponds to the breakage of horizontal bonds (Hazzard et al., 2000).

3.4.1. Opening mode of microcracks

As shown in Fig. 2c, the unit is subjected to a compressive force *Fz*. Horizontal bonds (such as bond 2) break in opening mode when the relative displacement between bottom elements (X_{n2}) exceeds the breaking displacement (X_b). Let C_{open} represents the magnitude of the vertical stress when the horizontal bonds break, which is comparable to the stress when micro-cracks formed in rock. Substituting Eq. (2d) into Eq. (5), C_{open} can be expressed as:

$$C_{open} = \frac{6\sqrt{2}\,K_n(K_n + K_s)}{K_n - K_s} \cdot \frac{X_b}{d^2} \tag{8}$$

3.4.2. Sliding mode of fracture plane

The failure of inclined bonds (such as bond 1) corresponds to the macroscopic shear fracture plane of laboratory specimens. In Fig. 2c, when bond 2 has broken, a vertical compressive force *Fz* acts on element 1, and horizontal compressive forces (such as *Fx*) act on bottom elements and toward the center point *O*. The force balance of element 2 requires that:

$$\begin{cases} F_{n1} = \sqrt{6}/9{\cdot}Fz + \sqrt{3}/3{\cdot}Fx \\ F_{S1} = \sqrt{3}/9{\cdot}Fz - \sqrt{6}/3{\cdot}Fx \end{cases} \tag{9}$$

With increasing vertical compressive force, inclined bonds will break when the magnitude of F_{S1} is equal to the maximum shear force allowed by Coulomb friction (Eq. (1)). Substituting Eq. (9) into Eq. (1) gives the following expression between *Fz* and *Fx*:

$$Fz = -\frac{3\sqrt{3}}{1-\sqrt{2}\mu_p}Fs_0 + \frac{3\sqrt{2}+3\mu_p}{1-\sqrt{2}\mu_p}\cdot Fx \tag{10}$$

where μ_p and Fs_0 are inter-element coefficient of friction and shear resistance, respectively. The normal stresses along the x-direction (σ_{xx}) and z-direction (σ_{zz}) are determined by:

$$\begin{cases}\sigma_{xx} = \sqrt{6}Fx/d^2\\ \sigma_{zz} = 2\sqrt{3}Fz/(3d^2)\end{cases} \tag{11}$$

where d is the edge length for the tetrahedral lattice unit. With Eq. (10), the relationship between σ_{xx} and σ_{zz} is:

$$\sigma_{zz} = -\frac{6}{1-\sqrt{2}\mu_p}\cdot\frac{Fs_0}{d^2} + \frac{2+\sqrt{2}\mu_p}{1-\sqrt{2}\mu_p}\cdot\sigma_{xx} \tag{12}$$

According to the Coulomb criterion, the stress state on the failure surface meets the following condition (Pollard and Fletcher, 2005, p.363):

$$\sigma_{zz} = -C_u + [(1+\mu_i^2)^{1/2} + \mu_i]^2\sigma_{xx} \tag{13}$$

where C_u is the uniaxial compressive strength; μ_i is the coefficient of internal friction. It is assumed that the Coulomb criterion is valid throughout the model. Then, the first- and second terms of Eq. (13) are equal to those of Eq. (12), and the C_u and μ_i can be defined by:

$$C_u = \frac{6}{1-\sqrt{2}\mu_p}\cdot\frac{Fs_0}{d^2} \tag{14}$$

$$\mu_i = \frac{P-1}{2\sqrt{P}},\quad P = \frac{2+\sqrt{2}\mu_p}{1-\sqrt{2}\mu_p} \tag{15}$$

The conversion formulas of element parameters to material properties are given in Eqs. (4), (6), (7) and (14), (15). By using the equations, the conversion formulas of material mechanical properties to element parameters can be derived, which are provided in Appendix B.

4. Energy conversion and energy conservation

4.1. Mechanical energy of model

Elastic potential energy (E_e) is the sum of the strain energy of normal- and shear springs of bonds (Mora and Place, 1998; Place and Mora, 1999):

$$E_e = 0.5\cdot K_n X_n^2 + 0.5\cdot K_s X_s^2 \tag{16}$$

where K_n and K_s are the inter-element normal stiffness and shear stiffness, respectively; and X_n and X_s are the corresponding relative displacements. The gravitational potential energy (E_g) of an element is:

$$E_g = mgh \tag{17}$$

where m is element mass, g is the acceleration of gravity, and h is the height above the reference level. Kinetic energy (E_k) of an element can be expressed as:

$$E_k = 0.5\cdot mv^2 \tag{18}$$

where m is element mass, v is element velocity.

4.2. Calculation of heat

4.2.1. Viscous heat

Seismic waves are always attenuated by friction, scattering etc., as they travel through rocks, and mechanical energy dissipates into heat (Hazzard et al., 2000). In the discrete element method, viscosity is used to damp the waves in the model, and to avoid buildup of kinetic energy in the isolated system (Finch et al., 2003; Mora and Place, 1993, 1994; Place et al., 2002). The viscous force ($\boldsymbol{F_v}$) is given by:

$$F_v = -\eta\bullet x' \tag{19}$$

where η is viscosity and x' is element velocity. As the time step of the simulation is very small, element velocity is assumed to be constant in a step. Viscous heat (Q_v) is generated during viscous damping, which can be calculated by:

$$Q_v = -\boldsymbol{F_v}\bullet\boldsymbol{dL} \tag{20}$$

where $\boldsymbol{dL}$ is the displacement of the element during current step.

4.2.2. Breaking heat

When an intact bond breaks, the spring force of the bond reduces, and elastic potential energy (E_e) of the inter-element normal spring and/or shear spring will dissipate into heat. If the inter-element normal force is tensile, the E_e of both normal and shear springs reduce to zero, and the reduced E_e can be calculated according to Eq. (16).

If the inter-element normal force is compressive, the intact bond will break in sliding mode, when the inter-element shear force tends to exceed the maximum shear force of the intact bond (F_{Smax}). Then, two elements will slip past each other, and the shear force reduces to the maximum shear force of the broken bond (F_{Smax}'). The elastic potential energy of the normal spring is unchanged when the intact bond breaks. Therefore, the reduced E_e is determined by shear force as:

$$E_e = 0.5\cdot(F_{S\,max}^2 - F_{S\,max}'^2)/K_s \tag{21}$$

where K_s is inter-element shear stiffness. The total breaking heat (Q_b) is the sum of the reduced elastic potential energy during the failure of bonds.

4.2.3. Frictional heat

Two elements begin sliding when the bond is broken and the magnitude of external force exceeds the maximum shear force of the broken bond. Frictional heat (Q_f) is generated during this process. When the time step of numerical simulation is very small, the variation of inter-element friction is linear. And Q_f can be defined as the product of average sliding friction and effective sliding distance (dS):

$$Q_f = |0.5\cdot(F_{s1} + F_{s2})\cdot dS| \tag{22}$$

where F_{s1} and F_{s2} are inter-element shear force (i.e. sliding frictions) respectively at the beginning and end of the current step, i.e. the maximum shear forces of the broken bond (F_{Smax}' of Eq. (4)); and dS is the effective sliding distance.

As shown in Fig. 3a, the element with broken bond is locked by static friction at point P. The center of the element is originally located at point O' (corresponds to dashed circle), when the shear spring is free and shear force (F_S) is zero. If an external tangential force (f) acts on the element, the shear spring will be compressed and the element center will move to point O (corresponds to solid line circle). However, the contact point is still locked at point P, when $F_S < F_{Smax}'$. Therefore, both the effective sliding distance (dS) and frictional heat are zero during elastic deformation.

Fig. 3b shows the schematic of the effective sliding distance, when the element slips on a frictional surface (surface of another element). The element is originally located at point O_1, which slides to point O_2 after a time step. As inter-element normal force increases, the shear force (i.e. frictional force) increases from F_{S1} to F_{S2}, and the inter-element shear relative displacement increases from Xs_1 to Xs_2. The effective sliding distance on the frictional surface equals the length of P_1P_2, which can be calculated by:

$$dS = dS' - (F_{s2} - F_{s1})/K_s \tag{23}$$

where dS' is the relative displacement of two elements along the shearing direction, i.e. O_1O_2 in Fig. 3b; K_s is the inter-element shear stiffness. Therefore, the effective sliding distance equals the tangential relative displacement of the element pair minus the reduction of spring

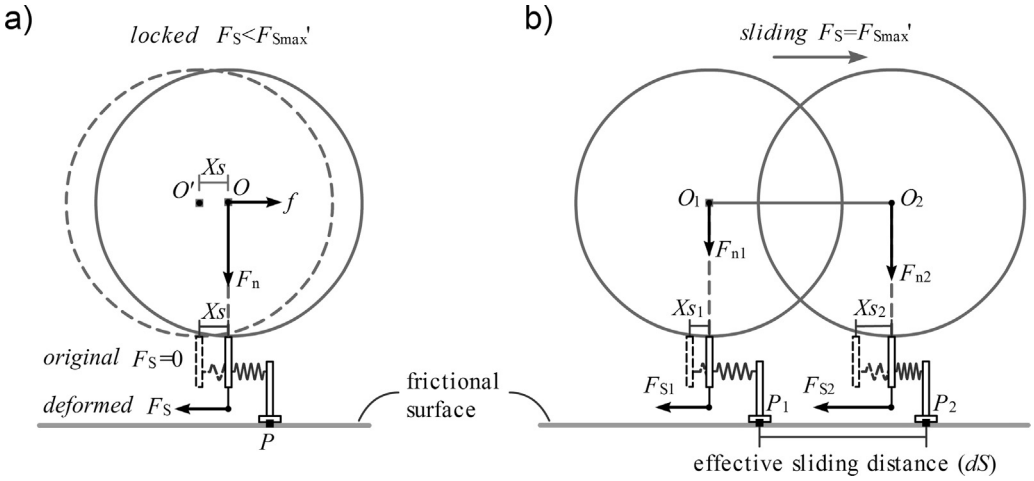

Fig. 3. Schematic of sliding distance used in the calculation of frictional heat. (a) The bond is broken and element is locked by static friction (i.e. $F_S < F_{Smax}'$). Although element center is moved to point O due to external force f, sliding distance along the contact surface is zero. (b) When the element slides, the effective sliding distance is the length of P_1P_2, which equals the tangential relative displacement (O_1O_2) of element pair minus the reduction of spring length (Xs_2-Xs_1).

length.

4.3. Energy conservation and external work

The heat in the model is the sum of viscous heat (Q_v), breaking heat (Q_b) and frictional heat (Q_f), which can be expressed as:

$$Q = Q_v + Q_b + Q_f \tag{24}$$

The total energy of a discrete element model is the sum of all mechanical energy and heat (Q):

$$E_{total} = E_e + E_g + E_k + Q \tag{25}$$

According to the law of conservation of energy, the total energy of an isolated system is constant. When the model deforms under external force. The increment of the total model energy must be equal to the work done by the external force (W_e). Specifically, when a model is compressed, the work of the external force is defined by:

$$W_e = 0.5\cdot(\mathbf{F_{b1}} + \mathbf{F_{b2}})\cdot\mathbf{dL} \tag{26}$$

where $\boldsymbol{F_{b1}}$ and $\boldsymbol{F_{b2}}$ are the force of the boundary before- and after a compressive step; $\boldsymbol{dL}$ is the displacement of the boundary.

5. Examples and validations

5.1. Numerical tests of 3D models of quartzite

On the basis of the theoretical study in this paper, a Matlab code "MatDEM^{3D}" has been developed and numerical models of quartzite were used to validate the formulas and the model. The mechanical properties of the quartzite and corresponding inter-element parameters of the close-packed model are shown in Table 1. The inter-element parameters of the models are calculated using the conversion formulas. Note that the density of the quartzite corresponds to overall density of the close-packed model. Therefore, similar to 2D model (Hardy and Finch, 2006), the element mass (m) of the 3D model is determined by:

$$m = \rho\cdot(\sqrt{2}\,d^3/2) \tag{27}$$

where ρ is the density of quartzite (2.650×10^3 kg/m^3); d is the element diameter. In the model, the element diameter (d) is 0.001 m, and the element mass is 1.874×10^{-6} kg.

The element parameters were used to define a series of cubic models, such as the model in Fig. 1a. The element numbers of the models are respectively 4 (single unit), 82, 255, 580, 1105, 2166, 5461, 10985, 18079, 37681, i.e. the element numbers along y-direction are 2, 4, 6, 8, 10, 12, 16, 20, 24, and 30, respectively. The cubic models are bounded by two smooth planes (no shear force) respectively on the top- and bottom sides (e.g. Fig. 1a). The viscosity (η) used in the numerical simulation is determined by the following semi-empirical equation:

$$\eta = \frac{d}{V^{1/3}}\bullet(8m\bullet K_n)^{1/2} \tag{28}$$

where d is the element diameter; V is the volume of model; and $(8m\bullet K_n)^{1/2}$ is the critical viscosity when an element is fixed on a rigid boundary. According to a series numerical tests, the kinetic energy of the model reduces at high rate by using the viscosity.

The resultant force acting on an element is the summation of the normal forces, shear forces, viscous force and gravity on the element. The dynamic evolution of the model is simulated by integrating their equation of motion using Newtonian physics and a time-stepping algorithm (Cundall and Strack, 1979; Potyondy and Cundall, 2004). As the time step is very small (1×10^{-8} s), the velocity and acceleration of an element are assumed to be constant within a time step, which allows the calculation of displacement, viscous force and heat of each element, etc.

In the numerical tests, the models were compressed or stretched step by step to detect the effective elastic modulus and strengths. The boundary displacement is very small to ensure high accuracy. In the tests of Young's modulus and Poisson's ratio, the inter-element breaking displacement and shear resistance are increased by 100 times to avoid the breakage of intact bonds, and the displacement of the boundary is 1.70×10^{-10} m in each compressive step. The values are respectively 1.70×10^{-10} m and 1.70×10^{-9} m for tests of tensile strength and compressive strength. After each compressive (or tensile) step, the model is run for 100 time steps to damp reflected waves from the two edges.

Table 1
Quartzite mechanical properties (Pollard and Fletcher, 2005, pp. 321, 343 and 361) and corresponding inter-element parameters (element diameter is 0.001 m).

Mechanical properties of quartzite		Inter-element parameters	
Young's Modulus (E)	90 GPa	Normal stiffness (K_n)	46.794×10^6 N/m
Poisson's ratio (υ)	0.16	Shear stiffness (K_s)	8.068×10^6 N/m
Uniaxial tensile strength (T_u)	25 MPa	Breaking displacement (X_b)	1.704×10^{-7} m
Uniaxial compressive strength (C_u)	252 MPa	Initial shear resistance (Fs_0)	18.452 N
Coefficient of intrinsic friction (μ_i)	1	Friction coefficient (μ_p)	0.3964

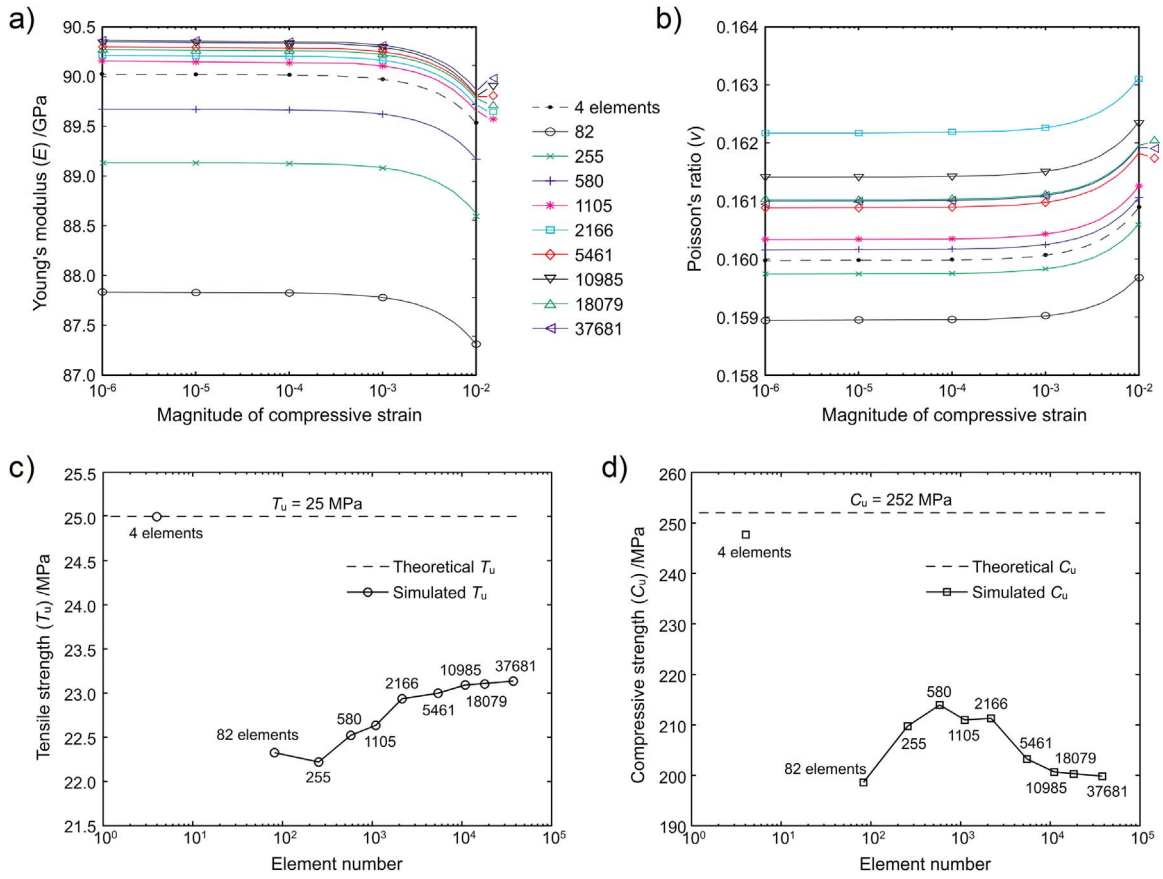

Fig. 4. Tested mechanical properties of close-packed models with different element numbers. (a) Young's modulus; (b) Poisson's ratio; (c) Uniaxial tensile strength (T_u); (d) Uniaxial compressive strength (C_u).

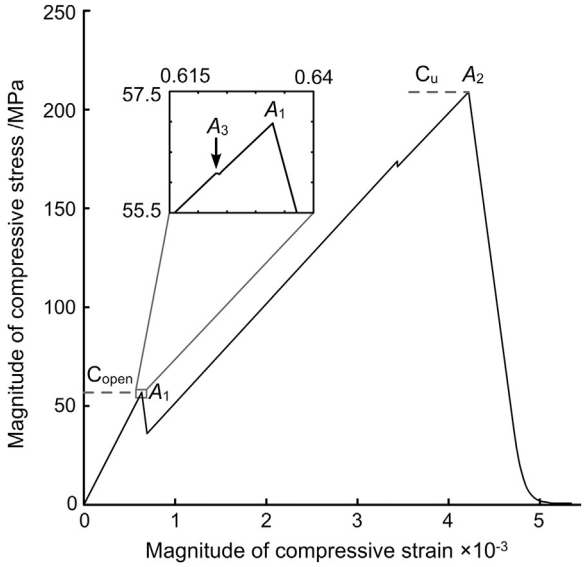

Fig. 5. Stress-strain curve of a compressive strength test of a cubic model with 2166 elements.

5.2. Test results of mechanical properties

Young's modulus (E) and Poisson's ratio (υ) of the models with different element numbers and different vertical strains are plotted respectively in Figs. 4a and b. When the compressive strain is -10^{-6}, the tested E and υ of a single unit coincide with the values of the quartzite, 90 GPa and 0.16. Because the derivation of the conversion formulas is based on small deformation assumption, the errors of elastic properties increase with increasing magnitude of strain. For models with multiple units, the average errors of E and υ from the strain -10^{-6} to -10^{-3} are about 0.6%.

Figs. 4c and d show the tested tensile strength (T_u) and compressive strength (C_u) of the models with different element numbers. The tested T_u and C_u of one unit are respectively 0.011% and 1.73% lower than the values of quartzite. The greater error of the C_u is related to the greater compressive strain ($>4\times10^{-3}$) in the C_u test. As shown in Fig. 4a, the error of Young's modulus also is greater when the strain exceeds 1×10^{-3}. For models with multiple units, the average tested T_u is 8.89% lower than corresponding theoretical value, and the average error of C_u is 18.51%. Because the conversion formulas are derived based on a single unit, the greater errors of multiple elements are related to the collective effect of an assemblage. Furthermore, due to the boundary effect, cracks are generally formed first around the boundaries in the numerical simulations. As shown in Fig. 1a, only one element is bonded with the boundary element P on its bottom side. The intact bond of the element will break prior to others, when the model is subjected to stress. Furthermore, the vertical stress is defined by the ratio of vertical force to the area of the model cross section. Due to the reduction of the number of effective boundary units, the tested T_u and C_u of models with multiple units are much smaller than the theoretical values.

The stress-strain curve of a uniaxial compressive strength test is shown in Fig. 5. In the test, the stress increases linearly from the origin to point A_1, where the microscopic opening cracks form, and as a result, the stress decreases. With increasing strain, the stress climbs up until reaching the uniaxial compressive strength (A_2), and after that the model fails in sliding mode. The inset figure shows the stress drops a bit at point A_3, which indicates some boundary bonds fail before the stress reaches C_{open}. And a drop of stress also can be found before the point A_2.

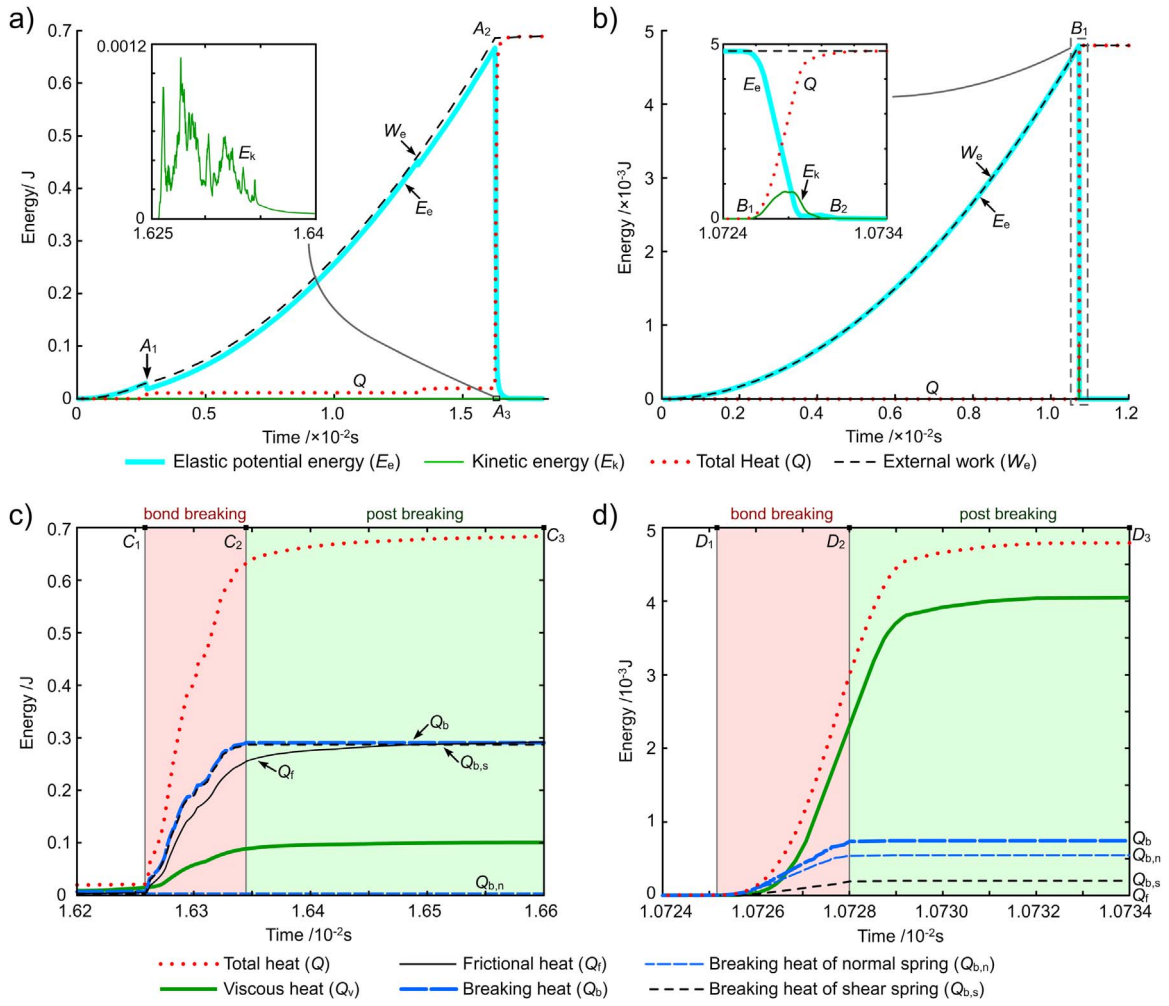

Fig. 6. (a) Energy curves of compressive strength (C_u) test. Inset figure shows variation of kinetic energy when the model fails. (b) Energy curves of tensile strength (T_u) test. Inset figure shows energy conversion when the model fails. (c) Heat curves when the model fails at point A_2 in Fig. 6a. (d) Heat curves when the model fails at point B_1 in Fig. 6b.

5.3. Test results of energy conversion

The cubic model with 2166 elements (i.e. 12 elements along y direction) is used as an example to show the energy conversion during the tests of compressive strength (C_u test) and tensile strength (T_u test). In the simulation, elastic potential energy, kinetic energy, heat and work of external force are calculated in each compressive step or tensile step. As the model is very small, gravitational potential energy is not considered, i.e. the acceleration of gravity is zero.

The energy curves of the C_u test are shown in Fig. 6a. The trend of the elastic potential energy (E_e) is similar to the stress-strain curve of Fig. 5. The E_e drops a bit at point A_1, where opening microcracks form and heat is generated. The whole model fails in sliding mode at point A_2, and E_e declines to almost zero at point A_3. The original energy of the model is zero. Therefore, the sum of mechanical energy and heat is always equal to external work (dashed line) during the simulation. The inset figure shows the variation of kinetic energy during the failure process, which takes about 1×10^{-4} s (second). As the elements are still compacted and inactive when the model fails, the kinetic energy is much smaller in comparison with the E_e and heat.

Fig. 6b shows the energy conversion of the T_u test. The model is stretched step by step until the model breaks into two halves at 1.072×10^{-2} s, where the stress is suddenly released and stored elastic potential energy (E_e) is converted into kinetic energy and heat. The inset figure shows the energy conversion curves for the failure process. When the model breaks at time B_1, E_e drops dramatically almost to zero. Part of the E_e is converted into breaking heat directly. The rest E_e is converted into kinetic energy, and elastic waves are generated in the model. As the failure surface is free in the T_u test, the model is more dynamic, and the ratio of maximum kinetic energy to total energy (16.2%) is greater than that of the C_u test (Fig. 6a). Finally, kinetic energy is converted into viscous heat at time B_2. However, the sum of the mechanical energy and heat is always equal to the external work.

Fig. 6c illustrates the variation of heat when the model fails in the C_u test (at point A_2 of Fig. 6a). The failure process starts at time C_1, when the element bonds break and the elements begin slipping toward each other. Elastic wave is generated in the model, and as a result viscous heat increases. The total breaking heat is the sum of breaking heat of normal spring ($Q_{b,n}$) and shear spring ($Q_{b,s}$). As the elements are compacted, the $Q_{b,n}$ is unchanged during the failure process, while the $Q_{b,s}$ increases when element bonds break step by step. As a result, the total breaking heat increases dramatically, until the whole model fails in sliding mode at time C_2. Beyond the time C_2, the breaking heat remains constant. However, the frictional heat still increases, which indicates element slipping along shear direction.

The heat variation of failure process of the T_u test is shown in Fig. 6d. The failure process of the model starts at time D_1 when the breaking heat increases from zero, and ends at time D_2 when the breaking heat stops increasing. The time difference between D_1 and D_2 is 2.83×10^{-6} s, and the model is 1.2 cm in width, therefore the propagation speed of the opening crack is about 4240 m/s. As the model is more dynamic in the T_u test, and the ratio of viscous heat to total heat is greater than that of C_u test. In Fig. 6d, the viscous heat still increases quickly after the model is completely broken at time D_2,

which indicates the strong elastic wave propagation in the model. There is no slipping when the model is split into two halves in the T_u test, so the frictional heat is always zero.

6. Discussion and conclusions

This paper gives the conversion formulas between the inter-element parameters and mechanical properties of 3D close-packed lattice model. The models of quartzite were used as an example to validate the conversion formulas and test the errors. The tested elastic properties and strengths of one unit correspond reasonably well with the values of quartzite. For models with multiple units, the average errors of E and υ are about 0.6%. However, tested T_u and C_u are lower than the values predicted by the formulas. Therefore, greater T_u and C_u can be used in the conversion formulas to counteract this effect. For example, the tested T_u is about 8.89% lower than the theoretical value, so the input T_u can be increased by 9.76% in the conversion formulas (Eq. (B3)), i.e. the X_b is increased by 9.76%. According to Eq. (14), C_u increases with increasing Fs_0 and μ_p, however, μ_i also is related to μ_p (Eq. (15)). Therefore, we can increase Fs_0 to get a greater C_u, and without influencing μ_i.

In the model, a discrete element does not represent a grain of rock, but the assemblage of the close-packed lattice has similar mechanical and dynamic behaviors as a rock block or a grain. If each grain of rock is represented by a close-packed lattice model, the deformation and failure of grains can be simulated (Cho et al., 2007; Mora and Place, 1998; Potyondy and Cundall, 2004). In order to simplify the model and reduce the computational cost, the shear force of the model is not applied at the surface, but at the center of each element. When a rock grain is represented by an element cluster, the grain can be rotated, and torque due to forces on surface elements will be modeled (Mora and Place, 1998). With the application of the conversion formulas introduced in this study, grains with specified mechanical properties can be used to construct rock models via sedimentation or other processes. As a result, the model also can be used to simulate the different packing, grain sorting, porosity of rock, and to investigate complicated structures that involve deformation and failure at both grain- and macroscopic scales. How the element clustering attributes and distributions influence the failure behaviors is an interesting future research topic.

The analytical solutions are applicable to a regular close-packed model. However, the disadvantage of the model is anisotropy (Place and Mora, 1999), and fracturing tends to occur along the planes of the unit (Fig. 2). In Fig. 2, the vertical force acts on the vertex A of the unit to test mechanical properties. As the unit is centrosymmetric, the mechanical properties of the unit along the directions from the unit center to the other three vertices also follow the formulas. Although we do not have analytical solutions of all the directions, some numerical tests indicate that the Young's modulus (E) and tensile strength (T_u) are a bit lower along other directions. Recently, Asahina et al. (2015) compare the result of the lattice model with the Finite Element Method. The lattice model can produce similar result as the traditional method (Fig. 8 of Asahina et al., 2015), which indicates the influence of anisotropy is not significant.

The rules of energy calculation and energy conversion are proposed to investigate the nonlinear dynamic process of rock. In the numerical tests, with the increasing boundary displacement, the total energy of the model increases step by step and always is equal to the work of external forces. When the model fails, stored stress energy is released and is converted into kinetic energy and heat. However, the sum of the mechanical energy and heat always remains constant. Variation of heat provides clues of failure processes, such as the speed of fracture propagation, and slipping behavior when the model breaks.

The model has been used to investigate the formation of wiggly compaction bands in porous sandstone (Liu et al., 2015). Further, the model can be used to investigate the dynamic processes, non-linear behaviors and heat generation during the evolution of structures, in particular, failure process of rock, faulting, earthquakes phenomena and dynamics, etc.

Acknowledgments

Data are available online: http://acei.cn/program/MatDEM. Financial supports from National Natural Science Foundation of China (41230636; 41302216), the National Science Found for Distinguished Young Scholars of China (41225011), Suzhou Science and Technology Program (SYG201614), and Open Fund of State Key Laboratory of Geohazard Prevention and Geoenvironment Protection (SKLGP2015K018) are gratefully acknowledged. Thanks to Professor David D. Pollard of Stanford University for his suggestions on this research. We are grateful to anonymous reviewers for many valuable suggestions that notably improved the manuscript.

Appendix A. Deformation of a single unit

In Fig. 2b, as the unit has a lateral triagonal symmetry, the normal- and shear relative displacements (X_{n1} and X_{s1}) between element 1 and the bottom elements are identical, and the normal relative displacements between the bottom elements (X_{n2}) also are the same. The inter-element normal- and shear spring forces of the unit can be defined as:

$$\begin{cases} F_{n1} = K_n \cdot X_{n1} \\ F_{S1} = K_s \cdot X_{s1} \\ F_{n2} = K_n \cdot X_{n2} \end{cases} \tag{A1}$$

where F_{n1}, F_{S1} are the normal- and shear forces between elements 1 and 2; F_{n2} is the normal force between elements 2 and 3. The right sides of the equations are corresponding stiffness and relative displacements. The force balance equations of the elements 1 (along z-axis) and 2 (along x-axis) are:

$$\begin{cases} Fz = 3 \cdot (F_{n1} \cdot \cos\alpha + F_{S1} \cdot \sin\alpha) \\ -F_{BO} = F_{n1} \cdot \sin\alpha - F_{S1} \cdot \cos\alpha \end{cases} \tag{A2}$$

where Fz is the vertical tensile force acted on the element 1 (Fig. 2b); F_{BO} is the resultant force of elements 3 and 4 on the element 2, therefore $F_{BO} = \sqrt{3} \cdot F_{n2}$;$\cos\alpha = \sqrt{6}/3$ and $\sin\alpha = \sqrt{3}/3$. The normal- and shear displacements between elements 1 and 2 are related to dz and X_{n2} as:

$$\begin{cases} X_{n1} = dz \cdot \cos\alpha + X_{BO} \cdot \sin\alpha \\ X_{s1} = dz \cdot \sin\alpha - X_{BO} \cdot \cos\alpha \end{cases} \tag{A3}$$

where the displacement of element 2 along BO direction is $X_{BO} = \sqrt{3}/3 \cdot X_{n2}$. There are seven independent variables (F_{n1}, F_{n2}, F_{S1}, X_{n1}, X_{n2}, X_{S1}, dz)

in the above seven linear equations. The equations can be solved using the regular linear algebraic method, and the solutions of dz, X_{n1}, X_{s1} and X_{n2} are provided in Eq. (2a-d). According to Eq. (A1), the F_{n1}, F_{n2} and F_{S1} can be calculated from X_{n1}, X_{s1} and X_{n2}.

Appendix B. Conversion formulas of material mechanical properties to inter-element parameters

Inter-element normal stiffness (K_n), shear stiffness (K_s), breaking displacement (X_b), shear resistance (Fs_0), coefficient of friction (μ_p) can be defined by Young's modulus (E), Poisson's ratio (v), tensile strength (T_u), compressive strength (C_u) and coefficient of intrinsic friction (μ_i):

$$K_n = \frac{\sqrt{2}Ed}{4(1-2v)} \tag{B1}$$

$$K_s = \frac{\sqrt{2}(1-5v)Ed}{4(1+v)(1-2v)} \tag{B2}$$

$$X_b = \frac{3K_n + K_s}{6\sqrt{2}K_n(K_n + K_s)} \cdot T_u \cdot d^2 \tag{B3}$$

$$Fs_0 = \frac{1-\sqrt{2}\mu_p}{6} \cdot C_u \cdot d^2 \tag{B4}$$

$$\mu_p = \frac{-2\sqrt{2}+\sqrt{2}I}{2+2I}, \quad I = [(1+\mu_i^2)^{1/2} + \mu_i]^2 \tag{B5}$$

Appendix C. Supporting information

Supplementary data associated with this article can be found in the online version at doi:10.1016/j.cageo.2017.03.003.

References

Abe, S., Mair, K., 2009. Effects of gouge fragment shape on fault friction: new 3D modelling results. Geophys. Res. Lett., 36.

Asahina, D., Ito, K., Houseworth, J., Birkholzer, J., Bolander, J., 2015. Simulating the Poisson effect in lattice models of elastic continua. Comput. Geotech. 70, 60–67.

Boutt, D.F., McPherson, B.J.O.L., 2002. Simulation of sedimentary rock deformation: lab-scale model calibration and parameterization. Geophys. Res. Lett., 29.

Cho, N., Martin, C.D., Sego, D.C., 2007. A clumped particle model for rock. Int. J. Rock Mech. Min. 44, 997–1010.

Chu, S.S., Lin, M.L., Huang, W.C., Nien, W.T., Liu, H.C., Chan, P.C., 2015. Simulation of growth normal fault sandbox tests using the 2D discrete element method. Comput. Geosci.-Uk 74, 1–12.

Cundall, P.A., Strack, O.D.L., 1979. Discrete numerical-model for granular assemblies. Geotechnique 29, 47–65.

Dattola, G., di Prisco, C., Redaelli, I., Utili, S., 2014. A distinct element method numerical investigation of compaction processes in highly porous cemented granular materials. Int. J. Numer. Anal. Met. 38, 1101–1130.

Ergenzinger, C., Seifried, R., Eberhard, P., 2011. A discrete element model to describe failure of strong rock in uniaxial compression. Granul. Matter 13, 341–364.

Finch, E., Hardy, S., Gawthorpe, R., 2003. Discrete element modelling of contractional fault-propagation folding above rigid basement fault blocks. J. Struct. Geol. 25, 515–528.

Fournier, T., Morgan, J., 2012. Insights to slip behavior on rough faults using discrete element modeling. Geophys. Res. Lett., 39.

Griffiths, D.V., Mustoe, G.G.W., 2001. Modelling of elastic continua using a grillage of structural elements based on discrete element concepts. Int. J. Numer. Methods Eng. 50, 1759–1775.

Guo, Y., Morgan, J.K., 2007. Fault gouge evolution and its dependence on normal stress and rock strength - Results of discrete element simulations: gouge zone properties. J. Geophys. Res.-Sol. Ea, 112.

Guo, Y.G., Morgan, J.K., 2008. Fault gouge evolution and its dependence on normal stress and rock strength - Results of discrete element simulations: gouge zone micromechanics. J. Geophys. Res.-Sol. Ea, 113.

Hallbaue, Dk, Wagner, H., Cook, N.G.W., 1973. Some observations concerning microscopic and mechanical behavior of quartzite specimens in stiff, triaxial compression tests. Int. J. Rock. Mech. Min. 10, 713, (&).

Hardy, S., 2008. Structural evolution of calderas: insights from two-dimensional discrete element simulations. Geology 36, 927–930.

Hardy, S., Finch, E., 2006. Discrete element modelling of the influence of cover strength on basement-involved fault-propagation folding. Tectonophysics 415, 225–238.

Hardy, S., McClay, K., Munoz, J.A., 2009. Deformation and fault activity in space and time in high-resolution numerical models of doubly vergent thrust wedges. Mar. Pet. Geol. 26, 232–248.

Hazzard, J.F., Young, R.P., 2004. Dynamic modelling of induced seismicity. Int. J. Rock Mech. Min. 41, 1365–1376.

Hazzard, J.F., Young, R.P., Maxwell, S.C., 2000. Micromechanical modeling of cracking and failure in brittle rocks. J. Geophys. Res-Sol. Ea 105, 16683–16697.

Hoover, W.G., Ashurst, W.T., Olness, R.J., 1974. 2-dimensional computer studies of crystal stability and fluid viscosity. J. Chem. Phys. 60, 4043–4047.

Horii, H., Nematnasser, S., 1985. Compression-induced microcrack growth in brittle solids - axial splitting and shear failure. J. Geophys. Res.-Solid 90, 3105–3125.

Kazerani, T., Zhao, J., 2010. Micromechanical parameters in bonded particle method for modelling of brittle material failure. Int. J. Numer. Anal. Met. 34, 1877–1895.

Latham, S., Abe, S., Mora, P., 2006. Parallel 3-D simulation of a fault gouge using the lattice solid model. Pure Appl. Geophys. 163, 1949–1964.

Liu, C., Pollard, D.D., Shi, B., 2013. Analytical solutions and numerical tests of elastic and failure behaviors of close-packed lattice for brittle rocks and crystals. J. Geophys. Res.-Sol Ea 118, 71–82.

Liu, C., Pollard, D.D., Gu, K., Shi, B., 2015. Mechanism of formation of wiggly compaction bands in porous sandstone: 2. Numerical simulation using discrete element method. J. Geophys. Res.: Solid Earth 120, 8153–8168.

Michlmayr, G., Cohen, D., Or, D., 2013. Shear-induced force fluctuations and acoustic emissions in granular material. J. Geophys. Res.-Sol Ea 118, 6086–6098.

Mora, P., Place, D., 1993. A lattice solid model for the nonlinear dynamics of earthquakes. Int. J. Mod. Phys. C 4, 1059–1074.

Mora, P., Place, D., 1994. Simulation of the frictional stick-slip instability. Pure Appl. Geophys. 143, 61–87.

Mora, P., Place, D., 1998. Numerical simulation of earthquake faults with gouge: toward a comprehensive explanation for the heat flow paradox. J. Geophys. Res.-Sol Ea 103, 21067–21089.

Neveu, A., Artoni, R., Richard, P., Descantes, Y., 2016. Fracture of granular materials composed of arbitrary grain shapes: a new cohesive interaction model. J. Mech. Phys. Solids 95, 308–319.

Place, D., Mora, P., 1999. The lattice solid model to simulate the physics of rocks and earthquakes: Incorporation of friction. J. Comput. Phys. 150, 332–372.

Place, D., Lombard, F., Mora, P., Abe, S., 2002. Simulation of the micro-physics of rocks using LSMearth. Pure Appl. Geophys. 159, 1911–1932.

Pollard, D.D., Fletcher, R.C., 2005. Fundamentals of Structural Geology. Cambridge University Press, Cambridge, UK; New York.

Potyondy, D.O., Cundall, P.A., 2004. A bonded-particle model for rock. Int. J. Rock Mech. Min. 41, 1329–1364.

Potyondy, D.O., Cundall, P.A., Lee, C.A., 1996. Modelling rock using bonded assemblies of circular particles. Rock Mech. Tools Tech. Vols 1 and 2, 1937–1944.

Schopfer, M.P.J., Abe, S., Childs, C., Walsh, J.J., 2009. The impact of porosity and crack density on the elasticity, strength and friction of cohesive granular materials: insights from DEM modelling. Int. J. Rock Mech. Min. 46, 250–261.

Tavarez, F.A., Plesha, M.E., 2007. Discrete element method for modelling solid and particulate materials. Int. J. Numer. Methods Eng. 70, 379–404.

Virgo, S., Abe, S., Urai, J.L., 2013. Extension fracture propagation in rocks with veins: Insight into the crack-seal process using Discrete Element Method modeling. J. Geophys. Res.-Sol Ea 118, 5236–5251.

Wang, Y.C., Mora, P., 2008. Macroscopic elastic properties of regular lattices. J. Mech. Phys. Solids 56, 3459–3474.

Wang, Y.C., Yin, X.C., Ke, F.J., Xia, M.F., Peng, K.Y., 2000. Numerical simulation of rock failure and earthquake process on mesoscopic scale. Pure Appl. Geophys. 157, 1905–1928.

Yin, H.W., Zhang, J., Meng, L.S., Liu, Y.P., Xu, S.J., 2009. Discrete element modeling of the faulting in the sedimentary cover above an active salt diapir. J. Struct. Geol. 31, 989–995.